Resonant torus-assisted tunneling

Chang-Hwan Yi,[1,*] Hyeon-Hye Yu,[2] and Chil-Min Kim[1,†]
[1]*Department of Emerging Materials Science, DGIST. Hyeonpung-myeon Dalseong-gun, Daegu 711-873, Korea*
[2]*Department of Physics, Sogang University, Seoul, 121-742, Korea*
(Received 28 April 2015; revised manuscript received 18 October 2015; published 4 January 2016)

We report a new type of dynamical tunneling, which is mediated by a resonant torus, i.e., a nonisolated periodic orbit. To elucidate the phenomenon, we take an open elliptic cavity and show that a pair of resonances localized on two classically disconnected tori tunnel through a resonant torus when they interact with each other. This so-called resonant torus-assisted tunneling is verified by using Husimi functions, corresponding actions, Husimi function distributions, and the standard deviations of the actions.

DOI: 10.1103/PhysRevE.93.012201

I. INTRODUCTION

The term *scar* was first coined by Heller in 1984 to explain the unexpected localization of eigenfunctions on classical unstable periodic orbits in a stadium-shaped billiard [1]. Since then, numerous studies have been theoretically and experimentally made and scars found not only in closed systems such as chaotic billiards [1–6], hydrogen atoms in a magnetic field [7,8], a cold atom [9], molecular systems [10–14], and a microwave [15–18] but also in open systems such as quantum dots [19–21] and optical microcavities [22–31]. In a quantum-mechanical point of view, a scar is a quantum-mechanical mixing of a pair of eigenfunctions due to an avoided level crossing (ALC), which is the phenomenon of Fermi resonance [14,32–35]. Recently, such abnormal scars have been found in dielectric microcavities as a quasiscarred resonance [23,25] and a scar-like one [36]. A quasiscar appearing in a spiral-shaped microcavity is a linear combination of a series of resonances [25] and a scar-like resonance is caused by an avoided resonance crossing (ARC) between two resonances [34,37], which is an open version of an ALC.

Along with scars, dynamical tunneling [38,39] has been extensively studied and several variations have been found. Through the studies, it has been verified that dynamical tunneling is also a quantum-mechanical mixing of a pair of eigenfunctions [34,36,37], which is now a phenomenon of Fermi resonance due to interaction of a pair of eigenfunctions. For mixing, a pair of eigenfunctions localized on classically disconnected regions tunnel either through a chaotic region, which is called chaos-assisted tunneling [40–44], or through classical resonances, which is called resonance-assisted tunneling [42–46].

In interaction of a pair of eigenfunctions, there are two types of ALCs, the Landau-Zener type [47,48] and the Demkov type [49]. In the former, an ALC takes place in a narrow range and the properties of a pair of eigenfunctions are recovered after the ALC, which is dynamical tunneling. In the latter, an ALC takes place over a broader range and a pair of scars are generated, which is scar formation [11]. In the formation of a scar-like resonance in an elliptic microcavity, an ARC takes place in a narrow range and the properties of a pair of resonances are recovered after an ARC [36]. Notwithstanding this commonness with dynamical tunneling in characteristics, a scar-like resonance has been regarded as a kind of scar [36,37]. Refuting this general understanding, in this paper, we will prove that a scar-like resonance is not a kind of scar but a phenomenon of dynamical tunneling assisted by a resonant torus, i.e., a nonisolated periodic orbit. To study this new type of dynamical tunneling, i.e., what we call resonant torus-assisted tunneling, we take an elliptic dielectric microcavity and show that a pair of remote resonances tunnel through a resonant torus.

II. ELLIPTIC MICROCAVITY

The shape of an elliptic microcavity is given by

$$x^2 + \frac{y^2}{1-\varepsilon^2} = a^2, \tag{1}$$

where a is the radius of the major axis and ε is the eccentricity. In an ellipse, two foci are at $f = \pm a\varepsilon$ and the radius of the minor axis is $b = \sqrt{a^2 - f^2}$. To prove the resonant torus-assisted tunneling, we obtain eigenvalue spectra and resonances depending on ε by solving the Helmholtz equation by the boundary element method for a refractive index $N = 3.3$ [50]. As a circular microcavity deforms, complicated interactions take place. Of these, we choose an arbitrary Landau-Zener-type ARC and investigate the characteristics of a pair of resonances during the interaction.

Figure 1 is the phenomenon of the interaction of the $(l,m) = (9,9)$ and the $(7,15)$ resonance, where l and m are the hyperbolic and the elliptic quantum number in elliptic coordinate, respectively. Figures 1(a) and 1(b) are the real and the imaginary eigenvalues of the two resonances as a function of ε, respectively, which show an ARC in a narrow range. Here k is the vacuum wave number and $R = \sqrt{ab}$. In order to show the Landau-Zener-type ARC, intensity plots of resonances are obtained for three cases of ε around the ARC. Interacting with each other, the $(9,9)$ and the $(7,15)$ resonance shown in Figs. 1(c) and 1(d) at $\varepsilon = 0.6$ develop to a pair of scar-like resonances as shown in Figs. 1(e) and 1(f) at $\varepsilon = 0.632$, respectively. After the ARC, the original resonances are recovered exchanging their properties as shown in Figs. 1(g) and 1(h) at $\varepsilon = 0.66$, respectively. This is an evidence of the Landau-Zener-type ARC.

*yichanghwan@hanmail.net
†chmkim@dgist.ac.kr

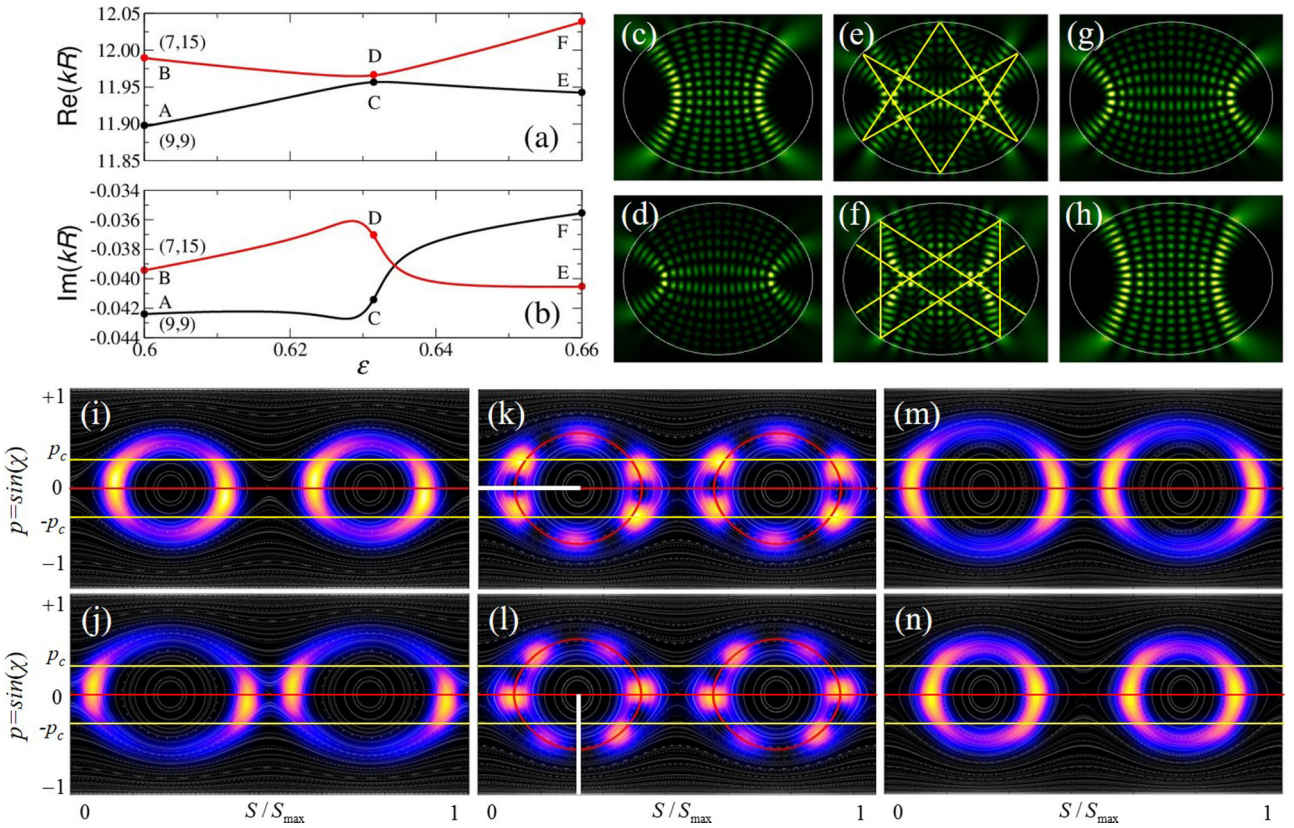

FIG. 1. Avoided resonance crossing, resonances, and Husimi functions depending on ε. (a) and (b) are the real and the imaginary eigenvalues of the (9,9) and the (7,15) resonance, respectively. (c) and (d) are the intensity plots of the (9,9) and the (7,15) resonance at $\varepsilon = 0.6$ [A and B in (a) and (b)], respectively. (e) and (f) are scar-like resonances at 0.632 (C and D), respectively. (g) and (h) are recovered resonances exchanging their property at 0.66 (E and F), respectively. (i) and (j) are the Husmimi functions of the (9,9) and the (7,15) resonance at $\varepsilon = 0.6$, respectively; (k) and (l) are those at 0.632 (C and D), respectively; and (m) and (n) are those at 0.66 (C and D). The bar in (k) and (l) are the cross section through one of the zeros of the Husimi functions. $S/S_{\max}$, $p = \sin(\chi)$, and p_c are the normalized arc length measured from positive x axis, the tangential component of a moment for a particle having an incident angle χ with respect to the normal vector at the system boundary, and the critical angle for a total internal reflection in a dielectric system of a refractive index $N = 3.3$, respectively.

III. FERMI RESONANCE AND SCAR-LIKE RESONANCE

In the interaction, because the two real eigenvalues are nearly degenerated, a Hamiltonian $H(I_1', I_2')$ can be expanded around the other one $H(I_1, I_2)$, where I_i and I_i' are the action variables and the subscripts 1 and 2 are the degrees of freedom. Then we can obtain the following condition:

$$(I_1 - I_1')\omega_1 + (I_2 - I_2')\omega_2 = 0, \tag{2}$$

where $\omega_i = \partial H/\partial I_i$ is the frequency associated with the action I_i. When the winding number ω_1/ω_2 is rational such that $\omega_1/\omega_2 = r/q$, where r and q are integers, the orbit is periodic [51]. By using the condition $I_i = (n_i + \alpha_i/4)h$, where α_i is the Maslov index, we can obtain the following relation:

$$(|\Delta n_1|, |\Delta n_2|) = (q, r), \tag{3}$$

where $|\Delta n_1| = |n_1 - n_1'|$ and $|\Delta n_2| = |n_2 - n_2'|$ are the quantum number difference on each degree of freedom and (q,r) denotes the classical periodic orbit [34]. Here we assume $h = 1$. In our case, because the quantum number difference is $(|\Delta l|, |\Delta m|) = (2,6)$, the scar-like resonances should be localized on the $(2:6)$ periodic orbits as we show the trajectories superimposed on the scar-like resonances.

To show localization of the scar-like resonance on the $(2:6)$ nonisolated periodic orbits, Husimi functions [52] are obtained for three cases of ε. The Husimi functions of the (9,9) and the (7,15) resonance shown in Figs. 1(i) and 1(j) at $\varepsilon = 0.6$ show a localization of the resonances on their own tori, which are disconnected in phase space. As ε increases, while the two resonances begin to interact with each other, the tori are fixed at their own position. Figures 1(k) and 1(l) show that each resonance is split into six clusters at $\varepsilon = 0.632$, which range over the two tori, while the tori are still disconnected. At an ARC point, the clusters are localized on the $(2:6)$ resonant torus as indicated by an ellipse in Figs. 1(k) and 1(l) at $\varepsilon = 0.632$. After the ARC, each resonance is now localized on the counterpart torus, which is the phenomenon of resonance exchange shown in Figs. 1(g) and 1(h). In this resonant torus-assisted tunneling, the $(2:6)$ resonant torus is the tunneling channel for mixing the (9,9) and the (7,15) resonance.

IV. ACTION BEHAVIOR IN TUNNELING

The resonant torus-assisted tunneling can be verified by using action variables. In elliptic coordinate, two conserved

quantities, the Hamiltonian (=E) and the product of two angular momenta about two foci, are given as follows [53,54]:

$$H = \frac{p_u^2 - p_v^2}{f^2(\cosh^2 u - \cos^2 v)} = E, \tag{4}$$

$$L_1 L_2 = \frac{p_u^2 \sinh^2 u - p_v^2 \sin^2 v}{\cosh^2 u - \cos^2 v}, \tag{5}$$

where the subscripts u and v are the hyperbolic and the elliptic axis, respectively, and p_u and p_v are the hyperbolic and the elliptic momentum, respectively. Here, the mass is assumed to be 1/2. From Eqs. (4) and (5), we can obtain the canonical momenta $p_u^2 = E(f^2 \sinh^2 u - \alpha)$ and $p_v^2 = E(f^2 \sin^2 v + \alpha)$, where $\alpha \equiv L_1 L_2 / E$ is the modified angular momentum product.

A. Birkhoff coordinate expression

To express the above variables in terms of Birkhoff coordinate, the quantity α is transformed as follows [53]:

$$\alpha = p^2(b^2 + f^2 \sin^2 v) - f^2 \sin^2 v, \tag{6}$$

where $b = a\sqrt{(1-\varepsilon^2)}$ and $p = p_v / \sqrt{p_u^2 + p_v^2}$ is the tangential component of the momentum of an incident point-like particle. Because $x = f \cosh u \cos v$, $y = f \sinh u \sin v$, and $\sqrt{p_u^2 + p_v^2} \equiv 1$, the variables in Eq. (6) are given as follows:

$$p = \sin(\chi),$$
$$u = \tanh^{-1}(b/a),$$
$$v = \tan^{-1}\left[\frac{y(s)\cosh(u)}{x(s)\sinh(u)}\right],$$

where s and p are the axes of Birkhoff-coordinate in Poincare surface of section, and χ is the incident angle of the particle on the boundary $u = \tanh^{-1} b/a$.

Then, the action of each variable can be deduced from the relations $I_u = \frac{1}{2\pi} \oint_{\mathbf{u}} p_u du$ and $I_v = \frac{1}{2\pi} \oint_{\mathbf{v}} p_v dv$ as follows:

$$I_u = \frac{\sqrt{E}}{\pi}\left[a \sin\phi - \frac{a}{f}\mathcal{F}(\phi,\kappa) - f\mathcal{E}(\phi,\kappa)\right], \tag{7}$$

$$I_v = \frac{2\sqrt{E}}{\pi}\left[\frac{\alpha}{f}\mathcal{F}\left(\frac{\pi}{2},\kappa\right) + f\mathcal{E}\left(\frac{\pi}{2},\kappa\right)\right], \tag{8}$$

where $\sin\phi = b/\sqrt{b^2 - \alpha}$, $\kappa = \sqrt{f^2 + \alpha}/f$, $E = (Nk)^2$, and the functions $\mathcal{F}(\theta,\kappa)$ and $\mathcal{E}(\theta,\kappa)$ are the elliptic integral of the first and the second kind, respectively. Because the quasiprobability distributions (Husimi function) spread on the (s,p) phase space, the expectation value of the action $I(s,p)$ and its standard deviation σ for u and v can be obtained as follows:

$$\langle I_{u,v} \rangle = \sum_{(s,p)} \frac{I_{u,v}(s,p) h(s,p)}{\sum_{(s,p)} h(s,p)},$$

$$\sigma_{u,v} = \sqrt{\langle I_{u,v}^2 \rangle - \langle I_{u,v} \rangle^2},$$

where $h(s,p)$ is the Husimi function. Hereafter, the term action is used for the expectation value of the actions obtained by the above equation.

Figure 2 shows actions in the region $0.60 < \varepsilon < 0.66$. In Fig. 2, the (2 : 6) resonant torus (dot-dashed lines) passes between two tori (dotted line), where the two resonances are localized. The dotted lines are obtained by fitting the actions of the two resonances before and after interaction. The figure shows that when the action of the resonant torus approaches the center of the two tori, that of each resonance begins to get away from its torus and moves to the counterpart torus by passing through the resonant torus. Each action of the (9,9) (solid lines) and the (7,15) resonance (dashed lines) collides with the resonant torus at about $\varepsilon \sim 0.630$ and $\sim$0.632, respectively. This moving is classically forbidden but quantum-mechanically allowed. This is the very phenomenon of dynamical tunneling through a resonant torus. The moving of resonances through the resonant torus is clearly shown in the Supplemental Material [55].

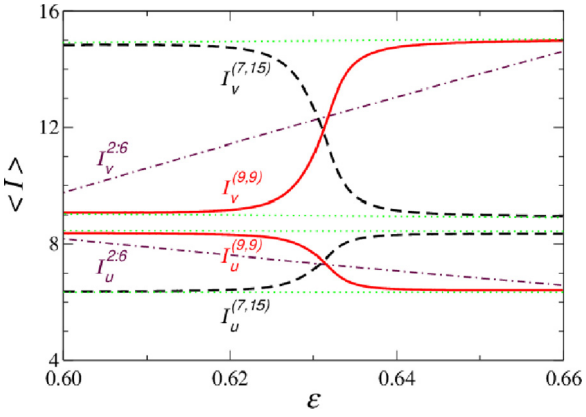

FIG. 2. Actions as a function of ε for each degree of freedom for the two interacting modes and the resonant torus. The dotted lines are the action tori, where the (9,9) and the (7,15) resonance are initially localized. The solid and the dashed lines are the action of the (9,9) and the (7,15) resonance, respectively. The dot-dashed lines are the actions of the (2 : 6) resonant torus. In numerical calculations of $I_{u,v}$ in Eqs. (7) and (8), energy is $E = \frac{1}{2}[(Nk)^2_{(9,9)} + (Nk)^2_{(7,15)}]$ and α is obtained by Eq. (6).

B. Husimi function and standard deviation behavior

The distribution variation of the Husimi functions on each section also clearly shows tunneling. We take the sections, which pass through the zeros of the Husimi function [10], as marked by a bar in Figs. 1(k) and 1(l). Figures 3(a) and 3(b) are the distribution of the Husimi function of the (9,9) and the (7,15) resonance on each section depending on ε. Before an ARC, the two resonances are distributed around their own tori as shown by the solid lines A and A′ in Figs. 3(a) and 3(b), respectively. As ε increases, each distribution begins to move to the counterpart torus as shown by the solid lines B and B′. Hence, during an ARC, the distribution is divided into two parts by the resonant torus: one part is on its own torus and the other on the counterpart torus, respectively. The position of the resonant torus is where the distribution is minimized between the two parts. Finally, when $\varepsilon = 0.66$, each distribution completely moves to the counterpart torus as shown by the solid lines C and C′. Due to the fact that the two resonances cannot be mixed through the zeros of

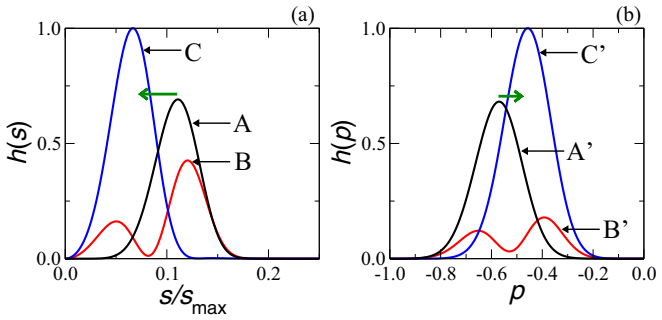

FIG. 3. Husimi function distributions depending on ε. (a) and (b) are the distributions at the sections shown in Figs. 1(k) and 1(l), respectively. A and A′ are at $\varepsilon = 0.6$, B and B′ at 0.628, and C and C′ at 0.66. Thick arrows in (a) and (b) indicate directions of the transition process.

the Husimi function, the distribution on the counterpart torus is certainly caused by the tunneling through the tunneling channels detouring the zeros of the Husimi function.

The standard deviations of the actions of the resonances as a function of ε are shown in Fig. 4. When dynamical tunneling takes place, a part of a resonance moves to the counterpart torus while the remaining part is kept on its own torus. Hence, the deviation becomes maximized when the tunneling of each resonance is maximized. Figure 4 shows the largest standard deviation around the ARC. The maximized positions are, approximately, $\varepsilon = 0.630$ and 0.632 for the (7,15) and the (9,9) resonance, respectively. The positions coincide with where the action of the resonant torus meets that of each resonance. This result implies that the tunneling of the (7,15) resonance is maximized earlier than that of the (9,9) resonance.

V. TUNNELING IN HIGH-ENERGY REGIME

In order to confirm the resonant torus-assisted tunneling at high-energy regime, we trace the eigenvalues around

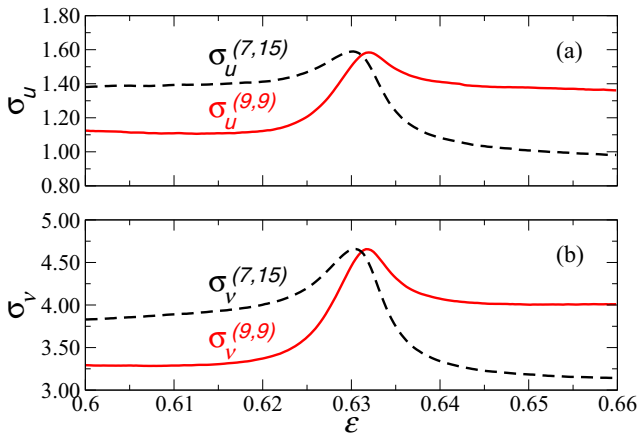

FIG. 4. Standard deviations of the Husimi function as a function of ε for two interacting resonances on each degree of freedom. The solid and the dashed lines are the (7,15) and the (9,9) resonance, respectively.

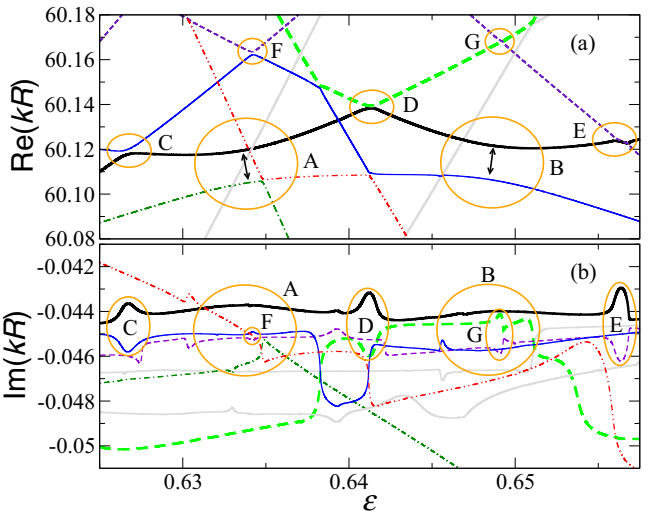

FIG. 5. Real and imaginary part of eigenvalues around $\mathrm{Re}(kR) \approx 60$ from $\varepsilon = 0.625$ to $\varepsilon = 0.6575$. Interaction pairs are marked by labeled circles of A, B, C, D, E, F, and G. Interacting pairs in regions A and B satisfy the (2, 6) Fermi resonance. C, D, and E satisfy the Fermi resonance 2(2, 6), and F and G satisfy the Fermi resonance 3(2, 6), respectively. The pairs in regions E and G are weak couplings and the others are strong couplings.

$\mathrm{Re}(kR) \approx 60$ for the eccentricity from $\varepsilon = 0.6250$ to $\varepsilon = 0.6575$. In Fig. 5, we can see several interaction pairs as labeled by A, B, C, D, E, F, G, and H.

A. Two-level non-hermitian approximation

When two eigenvalues interact with each other in an open nonequilibrium systems, the interaction can be expressed in the form of a 2×2 non-Hermitian matrix composed of a perturbed Hamiltonian as follows [56,57]:

$$\begin{aligned} H &= H_0 + \lambda H_1 \\ &= \begin{pmatrix} E_1 & 0 \\ 0 & E_2 \end{pmatrix} + \varepsilon U(\theta_1) \begin{pmatrix} \omega_1 & 0 \\ 0 & \omega_2 \end{pmatrix} U^\dagger(\theta_1) \\ &\quad + i\varepsilon U(\theta_2) \begin{pmatrix} \sigma_1 & 0 \\ 0 & \sigma_2 \end{pmatrix} U^\dagger(\theta_2) \\ &= \begin{pmatrix} H_{11} & H_{12} \\ H_{21} & H_{22} \end{pmatrix}, \end{aligned} \tag{9}$$

where

$$U(\theta) = \begin{pmatrix} \cos\theta & -\sin\theta \\ \sin\theta & \cos\theta \end{pmatrix},$$

and the eigenvalues of H are

$$\beta_\pm = \frac{H_{11} + H_{22} \pm \sqrt{(H_{11} - H_{22})^2 + 4H_{12}H_{21}}}{2}. \tag{10}$$

As is well known, the systems expressed by the above matrix exhibit three kinds of interactions: a strong, a weak, and an external coupling. The first case shows an avoided crossing in a real part of energy while an imaginary part of energy shows a crossing. The second case shows opposite behaviors to the first. In the last case of interaction, the imaginary part

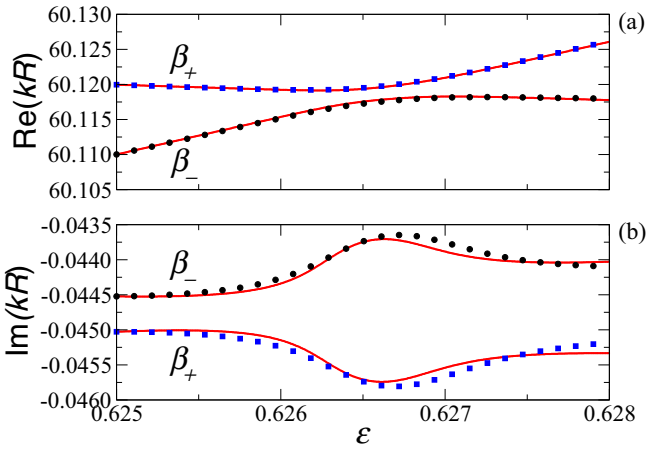

FIG. 6. Real and imaginary part of eigenvalues obtained by the numerical method and the model Hamiltonian of Eq. (9). In (a) and (b), filled squares and filled circles correspond to the thin solid lines of the resonance (36, 66) and the thick solid lines of the resonance (40, 54) in region C of Fig. 5, respectively. Solid lines $\beta_\pm$ in (a) and (b) are the real and imaginary part of eigenvalues in Eq. (10). The fitting eigenvalues are obtained using variables $E_1 = 60.11 - i0.0445$, $E_2 = 60.12 - i0.045$, $\theta_1 = 0.09$, $\theta_2 = 0.74$, $\omega_1 = 5.56$, $\omega_2 = -0.98$, $\sigma_1 = -0.62$, and $\sigma_2 = 0.68$.

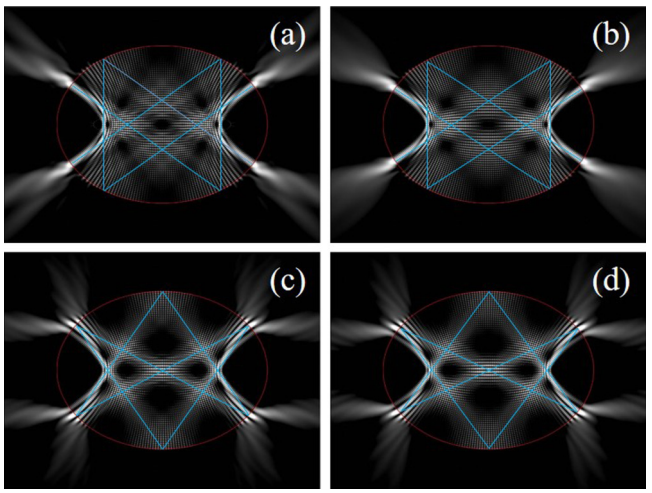

FIG. 7. Intensity plots of interaction pairs satisfying the $\mathcal{M}(2,6) = 1(2,6)$ Fermi resonance. (a) and (c) are (2, 6) scar-like resonances in region A of Fig. 5 at $\varepsilon = 0.634$ whose quantum numbers are (36, 66) and (38, 60) at $\varepsilon = 0.628$. (b) and (d) are those in region B of Fig. 5 at $\varepsilon = 0.648$ whose quantum numbers are (34, 72) and (36, 66) at $\varepsilon = 0.643$. $\mathcal{N}(2:6) = 1(2:6)$ periodic orbit family are superimposed on these resonances (thin solid lines).

of the energy shows a repulsion, resulting in one short and one long-lived resonance, while the real part of energy shows either crossings or avoided crossings. Hence, a direct measure of a tunneling rate using the gap of the avoided crossing is not tractable. The only applicable approach is to fit the parameter-dependent resonances using the eigenvalues of the model Hamiltonian, which is expressed by Eqs. (9) and (10).

Figure 6 is one example of the fitting for the interaction around region C in Fig. 5. The fitting eigenvalues are obtained using variables $E_1 = 60.11 - i0.0445$, $E_2 = 60.12 - i0.045$, $\theta_1 = 0.09$, $\theta_2 = 0.74$, $\omega_1 = 5.56$, $\omega_2 = -0.98$, $\sigma_1 = -0.62$, and $\sigma_2 = 0.68$. These are determined by using the approximated linear slopes of eigenvalues obtained by the numerical method. The tunneling strength can be identified by the mixing angles θ_1 and θ_2. In this case, off-diagonal elements H_{ij} at $\varepsilon \approx 0.6267$ are obtained to be $H_{12} = 0.000974 - i0.00107 = H_{21}$. The coupling strength of the resonant torus-assisted tunneling is determined by the boundary conditions which give complex values. Detailed discussions of the tunneling strength depending on k (or effective $1/\hbar$) and an interplaying of a resonant torus and the boundary conditions will be shown elsewhere.

B. Nonisolated avoided crossings

Figure 5 shows several kinds of interacting pairs. The pairs in regions A and B exhibit interactions over a wide range of eccentricity and show strong-external coupling. An analysis of these interactions is not easy since the interactions are not isolated (i.e., since multiple interactions take place simultaneously). For example, in region A, while the thick solid line interacts with the thin dotted dashed line, the thin double dotted dashed line interacts with the dotted dash line at $\varepsilon \approx 0.635$ simultaneously. Also, in region B, while the thick solid line interacts with the thin solid line, the gray thin line interacts with the thin solid line at $\varepsilon \approx 0.646$ simultaneously. Actually, many other small interactions take place during this wide-ranged interaction. However, because these small interactions do not distort the structures we are interested in and only appear in short-ranged local regions, we exclude them and concentrate on interactions satisfying the (2, 6) Fermi resonance.

The pairs in regions A and B satisfy the Fermi resonance (2, 6). For the pair in region A, a quantum number of the thick solid line and the dotted dashed line are (36, 66) and (38, 60), whose eigenfunctions are shown in Figs. 7(a) and 7(c), respectively. For the pair in region B, a quantum number of the thick solid line and the thin solid line are (34, 72) and (36, 66), whose eigenfunctions are shown in Figs. 7(b) and 7(d), respectively. The analysis of the actions and their standard deviations is not presented here, because of the complicating interactions, as stated above, which can mislead the genuine properties of these interactions.

C. Multiplicity of periodic orbits

More interesting phenomena arise in the other regions. The pairs in regions C, D, and E are governed by the quantum number difference $(|\Delta l|, |\Delta m|) = (4,12)$. This state can be divided by a factor 2 and this factor is interpreted as a multiplicity $\mathcal{M}$ of the primitive periodic orbit $(2:6)$, so that $(4,12) = 2(2,6) = \mathcal{M}(2,6)$. In Figs. 8(a)–8(c), we can distinguish three independent periodic orbits that exceed a multiplicity $\mathcal{M} = 2$. However, because the fish-shape orbits in these figures are topologically degenerated in phase space (the number of the points corresponding to the orbit on phase space are only 6, which is related to time-reversal propagation of the orbit), two fish-shape orbits should be counted to be one. On the other hand, because other orbits exhibit no degeneracy

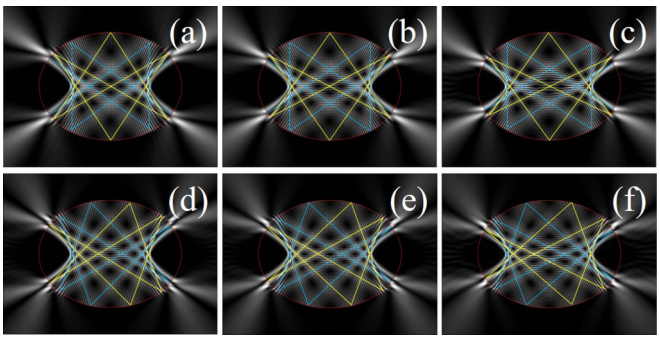

FIG. 8. Intensity plots of interaction pairs satisfying $\mathcal{M}(2,6) = 2(2,6)$ Fermi resonance. (a) and (d) are 2(2, 6) scar-like resonances in region C of Fig. 5 at $\varepsilon = 0.6267$ whose quantum numbers are (36, 66) and (40, 54) at $\varepsilon = 0.625$. (b) and (e) are those in region D of Fig. 5 at $\varepsilon = 0.6413$ whose quantum numbers are (34, 72) and (38, 60) at $\varepsilon = 0.6399$. (c) and (f) are those in region E of Fig. 5 at $\varepsilon = 0.6563$ whose quantum numbers are (32, 78) and (36, 66) at $\varepsilon = 0.6547$. $\mathcal{N}(2:6) = 2(2:6)$ periodic orbit family are superimposed on these resonances (thin solid lines).

in phase space, we count it as a complete one orbit. As a result, all pairs of scar-like resonances in Fig. 8 are defined to be (2, 6) having a multiplicity $\mathcal{M} = 2$. Simply, the orbit counting number $\mathcal{N}$ corresponding to the multiplicity $\mathcal{M}$ of Fermi resonance can be expressed in a following relation:

$$\mathcal{N} \equiv \sum_j \left(\frac{\frac{2}{g_j} \sum_1^n \delta[r'(s,p) - r(s,p)]}{2n} \right), \tag{11}$$

where g_j, n, and $r(s,p)$ are the degenerate factor, the bouncing number, and the position on phase space of jth periodic orbit, respectively. The degenerate factor g_j and factors 2 in Eq. (11) are related to time-reversal propagation of the orbit. For example, since the fish-shape orbit travels along the same points on phase space, g_j becomes 2 in time-reversed directions, while other orbits travel along different points in time-reversed directions on phase space for a period so that $g_j = 1$.

The first, the second, and the third column in Fig. 9 are actions and standard deviations of the interaction pairs in regions C, D, and E depending on eccentricity, respectively. The solid lines at each column are the (40, 54), the (38, 60), and the (36, 66) resonance, respectively. The dashed lines at each column are the (36, 66), the (34, 72), and the (32, 78) resonance, respectively. Dot dashed lines are the (2:6) resonant torus in each region. The first and the second row are the actions on each degree of freedom. The third and the fourth row are standard deviations on each degree of freedom. In the left two columns, the actions cross while the third one exhibits noncrossing behaviors. This is clearly comprehensible when we consider the properties of the weak coupling in the open systems. As mentioned before, when the weak coupling takes place, the real part of the eigenvalue crosses and the properties of the states are not exchanged while the strong coupling exchanges the properties of the states exhibiting an avoided crossing in the real part of eigenvalues.

Similarly, by using Eq. (11), $\mathcal{M} = 3$ interaction pairs in regions F and G in Fig. 5 are confirmed as shown in Fig. 10.

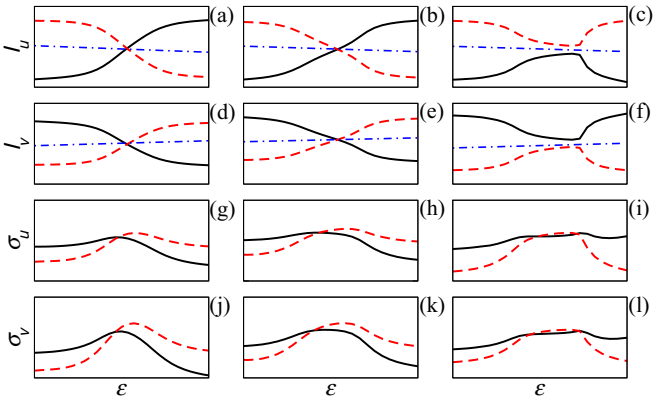

FIG. 9. Actions I_i and their standard deviations σ_i depending on eccentricity. The first, the second, and the third column are actions and standard deviations of the interaction pairs in regions C, D, and E depending on eccentricity, respectively. The solid lines at each column are the (40, 54), the (38, 60), and the (36, 66) resonance, respectively. The dashed lines at each column are the (36, 66), the (34, 72), and the (32, 78) resonance, respectively. Dot dashed lines are the (2:6) resonant torus in each region. The first and the second row are the actions on each degree of freedom. The third and the fourth row are standard deviations on each degree of freedom.

The pair in regions F and G exhibit Fermi resonance relations $|(34,72) - (40,54)| = 3(2,6)$ and $|(32,78) - (38,60)| = 3(2,6)$, respectively. Figure 11 shows actions and standard deviations of the actions of the pairs in regions F and the G depending on eccentricity. Again, the strong and the weak coupling properties are observed in the behaviors of actions and standard deviations.

By examining the behaviors of actions and standard deviations of all these interaction pairs, we summarize several

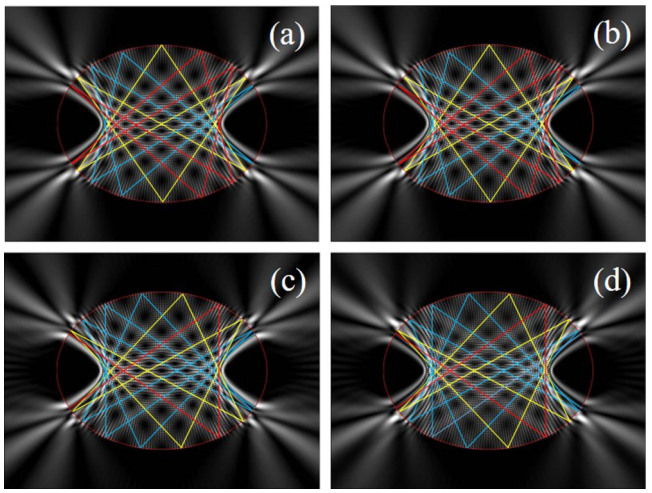

FIG. 10. Intensity plots of interaction pairs satisfying $\mathcal{M}(2,6) = 3(2,6)$ Fermi resonance. (a) and (c) are 3(2, 6) scar-like resonances in region F of Fig. 5 at $\varepsilon = 0.6342$ whose quantum numbers are (34, 72) and (40, 54) at $\varepsilon = 0.6331$. (b) and (d) are those in region G of Fig. 5 at $\varepsilon = 0.6492$ whose quantum numbers are (32, 78) and (38, 60) at $\varepsilon = 0.6478$. $\mathcal{N}(2:6) = 3(2:6)$ periodic orbit family are superimposed on these resonances (thin solid lines).

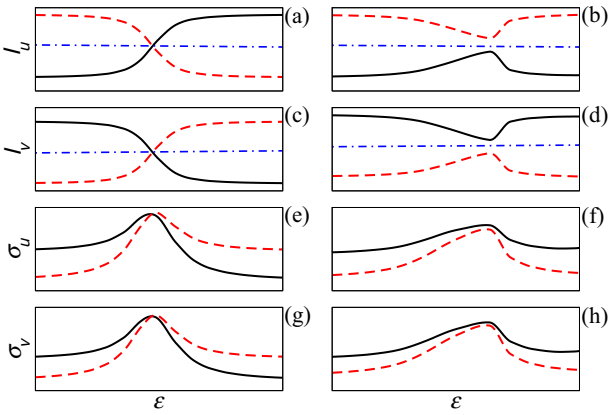

FIG. 11. Actions I_i and their standard deviations σ_i depending on eccentricity. The first and the second column are actions and standard deviations of the interaction pairs in regions F and G depending on eccentricity, respectively. The solid lines at each column are the (40, 54) and the (38, 60) resonance, respectively. The dashed lines at each column are the (34, 72) and the (32, 78) resonance, respectively. Dot dashed lines are the (2 : 6) resonant torus in each region. The first and the second row are the actions on each degree of freedom. The third and the fourth row are standard deviations on each degree of freedom.

important findings. First, now it is clear that the maximum points of the standard deviations of the interaction pairs do not coincide with each other. Although we tested the values expressed by a relative variance ($\sigma_{\text{rel}} = \frac{\sigma}{I}$), we were not able to deduce any meaningful clues for explaining it. Second, the actions and standard deviations depend on class of the coupling structure as shown in Figs. 9 and 11. Third, the actions of a resonant torus are placed at the center between the actions of the interacting pair. The concerns enumerated above will be addressed in rigorous and extensive ways in the future.

VI. BIFURCATION OF PERIODIC ORBIT

As a last remark, we point out the mechanism of a bifurcation and a developing of a resonant torus mediating interactions. The bouncing-ball-type resonant torus in an elliptic cavity is developed from a bouncing-ball orbit by a bifurcation. The "born" parameter is determined by the relation $\varepsilon = \cos[(q\pi)/r]$ [53,54]. After the generation of the resonant torus, as ε increases, the action on the v degree of freedom increases, whereas that on the u degree of freedom decreases as shown in Fig. 12. Hence, the action of the resonant torus can pass between a pair of tori, where a pair of resonances are localized. At this moment, when the Fermi resonance

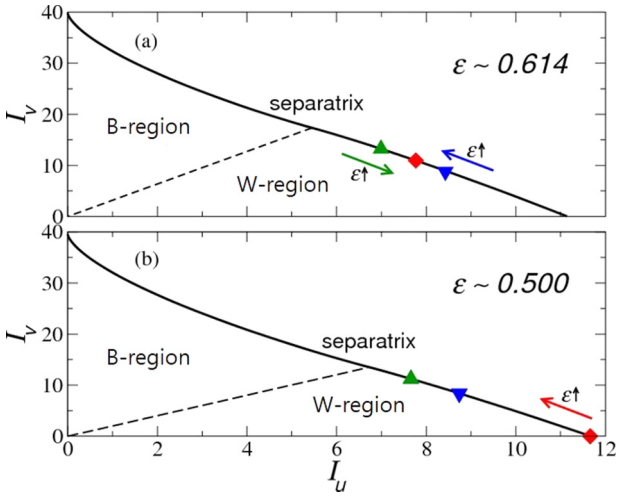

FIG. 12. Positions of two resonances (9, 9) and (7, 15) on the energy surfaces depending on eccentricity. The lower and the upper panel show resonance positions at $\varepsilon = 0.5$ and $\varepsilon = 0.614$, respectively. The upper triangle, the lower triangle, and the diamond symbol stand for the resonance (7, 15) and (9, 9), and the periodic orbit (2:6), respectively. Before $\varepsilon = 0.5$, the real (2:6) periodic orbit does not exist and has a negative I_v, which corresponds to an imaginary orbit. W and B region is a whispering gallery and a bouncing-ball-type region, respectively. The energy surfaces are obtained by using an arithmetic average of k squares of the interaction pair for energy E. α is ranged $-f^2 < \alpha < b^2$.

relation is satisfied, dynamical tunneling takes place through the resonant torus.

VII. CONCLUSION

In conclusion, we demonstrate a type of dynamical tunneling, which is resonant torus-assisted tunneling. This occurs when a resonant torus passes between a pair of tori. Although a pair of resonances, scar-like resonances, seem to be localized on a resonant torus, they are not scars, but the phenomenon of dynamical tunneling mediated by a resonant torus. This result will contribute to a deeper understanding of the widely prevailing phenomena of dynamical tunneling related to the interaction of a pair of eigenfunctions.

ACKNOWLEDGMENTS

This research was supported by Basic Science Research Program (NRF-2013R1A1A2060846) and High-Tech Convergence Technology Development Program (NRF-2014M3C1A3051331) through the National Research Foundation of Korea (NRF) funded by the Ministry of Science, ICT & Future Planning.

[1] E. J. Heller, Phys. Rev. Lett. **53**, 1515 (1984).
[2] O. Agam and S. Fishman, Phys. Rev. Lett. **73**, 806 (1994).
[3] Baowen Li, Phys. Rev. E **55**, 5376 (1997).
[4] F. P. Simonotti, E. Vergini, and M. Saraceno, Phys. Rev. E **56**, 3859 (1997).
[5] H. J. Stöckmann, *Quantum Chaos: An Introduction* (Cambridge University Press, London, 2000).
[6] K. F. Huang, Y. F. Chen, H. C. Lai, and Y. P. Lan, Phys. Rev. Lett. **89**, 224102 (2002).
[7] D. Delande and J. C. Gay, Phys. Rev. Lett. **59**, 1809 (1987).

[8] D. Wintgen and A. Hönig, Phys. Rev. Lett. **63**, 1467 (1989).
[9] J. Larson, B. M. Anderson, and A. Altland, Phys. Rev. A **87**, 013624 (2013).
[10] F. J. Arranz, F. Borondo, and R. M. Benito, Phys. Rev. E **54**, 2458 (1996).
[11] F. J. Arranz, F. Borondo, and R. M. Benito, J. Chem. Phys. **107**, 2395 (1997).
[12] A. M. Barr, K. Na, and L. E. Reichl, Phys. Rev. A **83**, 062510 (2011).
[13] M. Desouster-Lecomte and V. Jacquest, J. Phys. B **28**, 3225 (1995).
[14] Floyd L. Roberts and Charles Jaffé, J. Chem. Phys. **99**, 2495 (1993).
[15] S. Sridhar, Phys. Rev. Lett. **67**, 785 (1991).
[16] J. Stein and H.-J. Stöckmann, Phys. Rev. Lett. **68**, 2867 (1992).
[17] S. Sridhar and E. J. Heller, Phys. Rev. A **46**, R1728 (1992).
[18] S. Bittner, B. Dietz, R. Dubertrand, J. Isensee, M. Miski-Oglu, and A. Richter, Phys. Rev. E **85**, 056203 (2012).
[19] R. Akis, D. K. Ferry, and J. P. Bird, Phys. Rev. Lett. **79**, 123 (1997).
[20] Y. H. Kim, M. Barth, H. J. Stöckmann, and J. P. Bird, Phys. Rev. B **65**, 165317 (2002).
[21] M. Stopa, Physica B **249-251**, 228 (1998).
[22] T. Harayama, T. Fukushima, P. Davis, P. O. Vaccaro, T. Miyasaka, T. Nishimura, and T. Aida, Phys. Rev. E **67**, 015207(R) (2003).
[23] S. Y. Lee, S. R. Rim, J. W. Ryu, T. Y. Kwon, M. Choi, and C. M. Kim, Phys. Rev. Lett. **93**, 164102 (2004).
[24] S. Y. Lee, J. W. Ryu, T. Y. Kwon, S. Rim, and C. M. Kim, Phys. Rev. A **72**, 061801(R) (2005).
[25] J. Lee, S. Rim, J. Cho, and C. M. Kim, Phys. Rev. Lett. **101**, 064101 (2008).
[26] Q. Song, W. Fang, B. Liu, S. T. Ho, G. S. Solomon, and H. Cao, Phys. Rev. A **80**, 041807(R) (2009).
[27] C. H. Yi, S. H. Lee, M. W. Kim, J. Cho, J. Lee, S. Y. Lee, J. Wiersig, and C. M. Kim, Phys. Rev. A **84**, 041803(R) (2011).
[28] C. Gamachl, F. Capasso, E. E. Narimanov, J. U. Nöckel, A. D. Stone, J. Faist, D. L. Sivco, and A. Y. Cho, Science **280**, 1556 (1998).
[29] Edited by K. Vahala, *Optical Microcavities* (World Scientific, Singapore, 2004).
[30] J. U. Nöckel and A. D. Stone, Nature **385**, 45 (1997).
[31] H. H. Yu, C. H. Yi, and C. M. Kim, Opt. Express **23**, 11054 (2015).
[32] F. J. Arranz, F. Borondo, and R. M. Benito, Phys. Rev. Lett. **80**, 944 (1998).
[33] E. J. Heller, J. Phys. Chem. A **103**, 10433 (1999).
[34] C. H. Yi, H. H. Yu, J. W. Lee, and C. M. Kim, Phys. Rev. E **91**, 042903 (2015).
[35] B. Ramachandran and K. G. Kay, J. Chem. Phys. **99**, 3659 (1993).
[36] J. Wiersig, Phys. Rev. Lett. **97**, 253901 (2006).
[37] J. Unterhinninghofen, J. Wiersig, and M. Hentschel, Phys. Rev. E **78**, 016201 (2008).
[38] E. J. Heller, J. Phys. Chem **99**, 2625 (1995).
[39] M. J. Davis and E. J. Heller, J. Chem. Phys. **75**, 246 (1981).
[40] S. Lock, A. Backer, R. Ketzmerick, and P. Schlagheck, Phys. Rev. Lett. **104**, 114101 (2010).
[41] A. Backer, R. Ketzmerick, S. Lock, M. Robnik, G. Vidmar, R. Hohmann, U. Kuhl, and H. J. Stöckmann, Phys. Rev. Lett. **100**, 174103 (2008).
[42] A. Backer, S. Furstberger, and R. Schubert, Phys. Rev. E **70**, 036204 (2004).
[43] P. Schlagheck, A. Mouchet, and D. Ullmo, arXiv:1105.5362.
[44] C. Eltschka and P. Schlagheck, Phys. Rev. Lett. **94**, 014101 (2005).
[45] O. Brodier, P. Schlagheck, and D. Ullmo, Phys. Rev. Lett. **87**, 064101 (2001).
[46] O. Brodier, P. Schlagheck, and D. Ullmo, Ann. Phys. **300**, 88 (2002).
[47] L. D. Landau, Phys. Z. Sowjetunion **2**, 46 (1932).
[48] C. Zener, Proc. R. Soc. London A **137**, 696 (1932).
[49] Y. N. Demkov and V. I. Osherov, Sov. Phsy. JETP **26**, 916 (1968).
[50] J. Wiersig, J. Opt. A **5**, 53 (2003).
[51] M. Berry and M. Tabor, Proc. Roy. Soc. A **349**, 101 (1976).
[52] M. Hentschel, H. Schomerus, and R. Schubert, Europhys. Lett. **62**, 636 (2003).
[53] M. Sieber, J. Phys. A **30**, 4563 (1997).
[54] H. Waalkens, J. Wiersig, and H. R. dullin, Ann. Phys. (N.Y.) **260**, 50 (1997).
[55] See Supplemental Material at http://link.aps.org/supplemental/10.1103/PhysRevE.93.012201 for two videos.
[56] W. D. Heiss, Eur. Phys. J. D **7**, 1 (1999).
[57] W. D. Heiss, Phys. Rev. E **61**, 929 (2000).